Journal of Materials Chemistry C

PAPER

View Article Online
View Journal | View Issue

Cite this: J. Mater. Chem. C, 2019, 7, 1659

Ultrathin high-performance electromagnetic wave absorbers with facilely fabricated hierarchical porous Co/C crabapples†

Nannan Wu,[ab] Chang Liu,[a] Dongmei Xu,[c] Jiurong Liu,*[a] Wei Liu,[c] Hu Liu,[bd] Jiaoxia Zhang,[be] Wei Xie[f] and Zhanhu Guo[b]

Received 2nd October 2018,
Accepted 17th December 2018

DOI: 10.1039/c8tc04984j

rsc.li/materials-c

Extremely strong electromagnetic wave (EMW) absorption with a minimum reflection loss (RL) of −56.9 dB at 9.3 GHz at an absorber thickness of only 1.92 mm was observed for the hierarchical porous cobalt (Co)/carbon (C) crabapples, lab-made *via* a facile solvothermal reaction coupled with a following carbon reduction treatment. At an ultrathin thickness of 1.4 mm, the hierarchical porous Co/C crabapples (50 wt% filling content) provided 90% EMW absorption over a broad bandwidth of 5.9 GHz. A broad bandwidth of 5.8 GHz at 2.0 mm thickness was still achieved at a low filling ratio of 30 wt% filler content. This broad-band EMW absorption resulted from the synergy of cobalt and carbon with a significantly improved impedance matching level. The strong magnetism of cobalt endowed the composites with strong absorption ability and thin absorber thickness. The unique porous structural features also contributed to the enhanced EMW absorption by inducing multi-scatterings. The hierarchical porous Co/C crabapples with high absorbing performance together with ultrathin absorber thickness can be applied as a promising EMW absorption material.

1. Introduction

In recent years, with the ever-increasing usage of wireless devices and electronic instruments, electromagnetic interference (EMI) and electromagnetic wave (EMW) radiation have affected the normal operation of electronic devices and created great threats to human health.[1–5] To address the EMI and EMW radiation problems, high-performance EMW absorbing materials have drawn worldwide attention because of their capabilities to attenuate EM wave energy by converting it into thermal energy.[6–8] Commonly, ideal EMW absorption materials (named EMW absorbers) should possess the features of strong absorption capability, broad absorption bandwidth, thin matching thickness, and light weight. Among various kinds of absorbing materials, cobalt has attracted increasing attention because of its large permeability in the GHz range arising from its high saturation magnetization according to Snoek's limit $(\mu_s - 1)f_r = \frac{1}{3\pi}\gamma M_s$,[9,10] where γ is the gyromagnetic ratio, μ_s is the static permeability and M_s is the saturation magnetization value. Therefore, it is possible for cobalt to obtain a thin thickness at a certain frequency because of its high electric conductivity and enlarged permeability according to the quarter wavelength model $\left(d = nc/4f\sqrt{|\mu_r||\varepsilon_r|}\right)$,[11–13] in which ε_r is the complex permittivity, and the thickness d is inversely proportional to the complex permeability μ_r. Hence, cobalt materials with various morphologies and their EMW absorption properties were exploited. For example, porous hollow Co spheres exhibited an excellent EMW absorption with the minimum RL of −40 dB at 9.0 GHz due to the improved impedance matching between permittivity and permeability of the hollow structures.[14] Because of the high impedance matching and multi-scattering induced by the three-dimensional layered structure, the flower-like Co/CoO composites synthesized by Lv *et al.* presented outstanding EMW absorption with an optimal RL of −50 dB at 7.2 GHz.[11] Tong *et al.* designed a 3D

[a] Key Laboratory for Liquid-Solid Structural Evolution and Processing of Materials, Ministry of Education and School of Materials Science and Engineering, Shandong University, Jinan, Shandong 250061, China. E-mail: jrliu@sdu.edu.cn
[b] Integrated Composites Laboratory (ICL), Department of Chemical & Biomolecular Engineering, University of Tennessee, Knoxville, TN 37996, USA. E-mail: zguo10@utk.edu
[c] State Key Laboratory of Crystal Materials, Shandong University, Shandong 250100, China
[d] Key Laboratory of Materials Processing and Mold (Zhengzhou University), Ministry of Education, National Engineering Research Center for Advanced Polymer Processing Technology, Zhengzhou University, Zhengzhou, 450002, China
[e] School of Material Science and Engineering, Jiangsu University of Science and Technology, Zhenjiang, Jiangsu, 212003, China
[f] Key Laboratory of Lightweight and Reliability Technology for Engineering Vehicle, Education Department, Changsha University of Science & Technology, Changsha, Hunan, 410114, China

† Electronic supplementary information (ESI) available. See DOI: 10.1039/c8tc04984j

flower-like Co superstructure with a minimum RL of −40.25 dB at 6.08 GHz and the strong absorption was ascribed to enhanced dielectric ability and extra resonance behavior of the flower-like structures.[15] It can be concluded from the above reports that the microstructures have a crucial effect on the EMW absorption properties. Nowadays, considerable attention has been concentrated on the fabrication of EMW absorbers with large specific surface area and porous structures. On one hand, the abundant pores and defects on the large specific surface area can contribute to polarizations that lead to enhanced EMW absorption. On the other hand, the porous structure can scatter the incident EM waves and increase the EMW absorbing properties.[11,16] In addition, light-weight EMW absorbers can be obtained from the porous structures.

Except for the influences of EMW absorbers' microstructures, the balance between the complex permeability and complex permittivity (so-called impedance matching) plays crucial roles in determining the absorption performances.[17–19] For a single magnetic metal, it is quite difficult to attain impedance matching depending solely on magnetic loss and they are always suffering from a lot from drawbacks like ease of oxidation and high density, which restrict their practical utilizations. Currently, constructing nanocomposites composed of magnetic constituents and carbon materials is regarded as an effective approach to obtain high-efficiency EMW absorbers. These composites include Co_xNi_y/C nanocomposites,[20] Ni(C) nanocapsules,[21] Co@carbon nanotubes–graphene hybrids,[22] FeCo@C nanoflake composites[23] *etc.* On one hand, owing to a complementary effect of magnetic components and carbon, the impedance matching is improved significantly, resulting in enhanced EMW absorption compared with their individual constituents. On the other hand, the hetero-interfaces between different components can provide interfacial polarizations, further enhancing the EMW absorption ability. Various methods have been attempted to synthesize EMW absorbers composited with magnetic metals and carbon materials. Ni(C) nanocapsules have been synthesized successfully using a modified arc-discharge approach under a methane atmosphere.[21] FeCo@C nanoflakes were prepared through a two-step strategy including the reduction of Fe^{2+} and Co^{2+} by hydrazine hydrate and then calcinating a mixture of FeCo and glucose under an argon atmosphere.[23] Jiang *et al.* reported an arc-discharge technique to synthesize Co/Ni@SWCNTs nanocomposites.[24] In addition, some other methods, including arc plasma,[25] chemical vapor deposition (CVD)[26] and γ-ray irradiation[27] have also been adopted to prepare magnetic metal/carbon composite absorbents. It should be noted that during these synthetic processes, special devices, rigorous conditions or toxic reducing agents were always demanded. Therefore, developing a more facile and easily-extended route to fabricate magnetic metals/carbon composite absorbents is still in high demand.

In this study, hierarchical porous Co/C crabapples with average sizes of 4–7 μm were synthesized through a solvothermal reaction and following carbon reduction (CR) treatment. Structures and morphologies of the hierarchical porous Co/C crabapples were characterized. EMW absorption properties of the hierarchical porous Co/C crabapples were evaluated based on the measured μ_r and ε_r from 1.0–18.0 GHz. The hierarchical Co/C crabapples displayed superior EMW absorption as compared to many previously reported Co and Co/C composites. The mechanisms affecting their EMW absorption were investigated considering the synergistic effects between multiple components and their structural characteristics in detail.

2. Experimental section

2.1 Materials

Cobalt acetate ($Co(CH_3COO)_2{\cdot}4H_2O$), polyvinyl-pyrrolidone (PVP, K30) and pyrrole (C_4H_5N) were purchased from Sigma-Aldrich.

2.2 Fabrication of hierarchical porous Co/C crabapples

The synthetic process contains multi-step procedures. Typically, 2 mmol of $Co(CH_3COO)_2{\cdot}4H_2O$ and 2.0 g of PVP were dispersed in methanol (40 mL) at room temperature. The resulting solution was then transferred into a 60 mL Teflon-lined steel autoclave and heated at 180 °C for 3 h. After that, the pink precipitate was rinsed with distilled water and finally dried at 60 °C for 12 h. Crabapple-like Co_3O_4 was prepared through calcinating the above precipitate at 350 °C for 3 h in air. The CR treatment was carried out through injecting 1.0 mL of pyrrole into 1.5 g of Co_3O_4 intermediate in a tightly sealed steel autoclave and heated at 550 °C for 7 h.

2.3 Characterization

The morphology and microstructure of the products were characterized using JSM-6700F scanning electron microscopy (SEM) and transmission electron microscopy (TEM, JEOL JSM-2100). The X-ray powder diffraction (XRD) patterns of the samples were recorded using an XRD instrument with Cu Kα radiation in the scanning range of 10° to 90°. The room temperature hysteresis loops of the samples were recorded using a vibrating sample magnetometer (VSM, Lake Shore 7400). For the measurement of EM parameters, the as-obtained Co/C powders were homogeneously dispersed in epoxy resin. The filling ratio of sample was fixed at 50 wt% and 30 wt%, which were defined as samples M_{50} and M_{30}, respectively. Then, the mixture was cut into toroid-shaped samples (Φ_{out}: 7.00 mm, Φ_{in}: 3.04 mm). The *S* parameters of the samples were measured by using an Agilent N5232A vector network analyzer (VNA, USA) from 1.0–18.0 GHz by adopting the coaxial-line method. Then, software (Agilent Technologies 85071) installed in VNA was used to calculate the ε', ε'', μ' and μ'' values (Scheme 1).

3. Results and discussion

The preparation of hierarchical porous Co/C crabapples consists of three steps (Scheme 1). The crabapple-like α-$Co(OH)_2$ precursor was firstly synthesized following a solvothermal method. Then, the Co_3O_4 intermediate was obtained in the following calcination treatment. Finally, in the step of carbon reduction, the hierarchical porous Co/C crabapples were

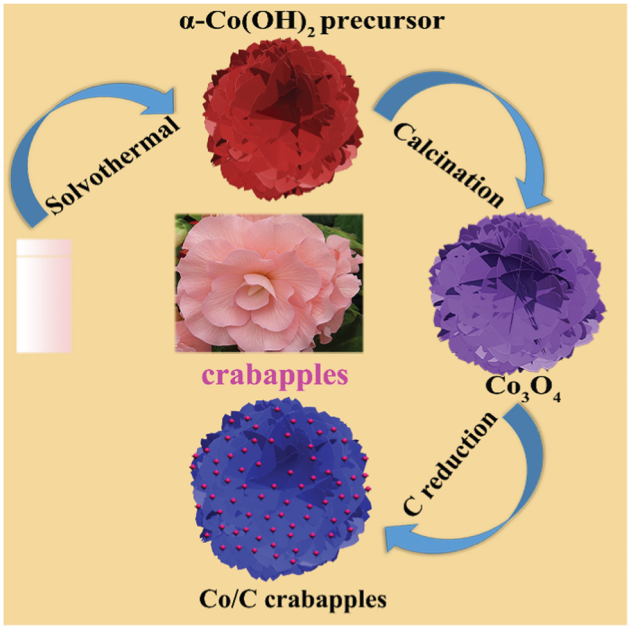

Scheme 1 Schematic formation process of porous Co/C crabapples.

produced with pyrrole as the carbon source. The carbon sheets were formed due to the connection of carbon and the reduced Co nanoparticles grew gradually with increasing temperature during the carbon reduction treatment. Therefore, pyrrole played a dual role during the synthesis of hierarchical Co/C crabapples. At first, it served as a reductant. Pyrrole liquids would be evaporated first and then absorbed on the Co_3O_4 crabapple surface. When the heating temperature reached 550 °C under the high pressure, carbon was produced from the pyrolysis of pyrrole and Co_3O_4 was reduced to Co. Simultaneously, a carbon layer on the Co nanoparticles and a carbon sheet were formed.

Fig. S1a (ESI†) shows the SEM images of the α-$Co(OH)_2$ precursor. A hierarchical crabapple-like architecture was observed with the size in the range of 4–7 μm. By magnifying an individual α-$Co(OH)_2$ crabapple, each crabapple-like structure is found to be self-assembled by abundant two-dimensional (2D) sheets (Fig. S1b, ESI†). After calcining in air, the Co_3O_4 intermediate is observed to maintain the morphology of the precursor (Fig. S1c, ESI†). The low magnification SEM and TEM images (Fig. 1a and Fig. S1d, ESI†) show that the hierarchical porous Co/C crabapples possess a size range of 4–7 μm. Although the amplified SEM image of an individual Co/C crabapple reveals no significant differences in both shape and size between Co/C crabapple and Co_3O_4 intermediate, a great number of tiny nanoparticles appeared on the sheets (Fig. 1b). The diameters of these nanoparticles are between 20–100 nm and numerous pores or defects were found to exist on the sheets simultaneously (Fig. 1c). To uncover the compositions of the nanoparticles and 2D sheets, elemental mappings were performed and the results are shown in Fig. S2 (ESI†). It can be concluded that the composites were made up of Co and C elements. The elemental distribution is quite uniform, illustrating the uniform growth of Co NPs on carbon frameworks. The TEM image in Fig. 1d confirms the amorphous 2D carbon sheets and these Co NPs in the range of 20–50 nm are coated by a thin layer. The lattice fringe spacing of 0.177 nm (inset of Fig. S1e, ESI†) observed for the nanoparticles matches well with (200) plane of fcc cobalt,[28] confirming that the nanoparticles

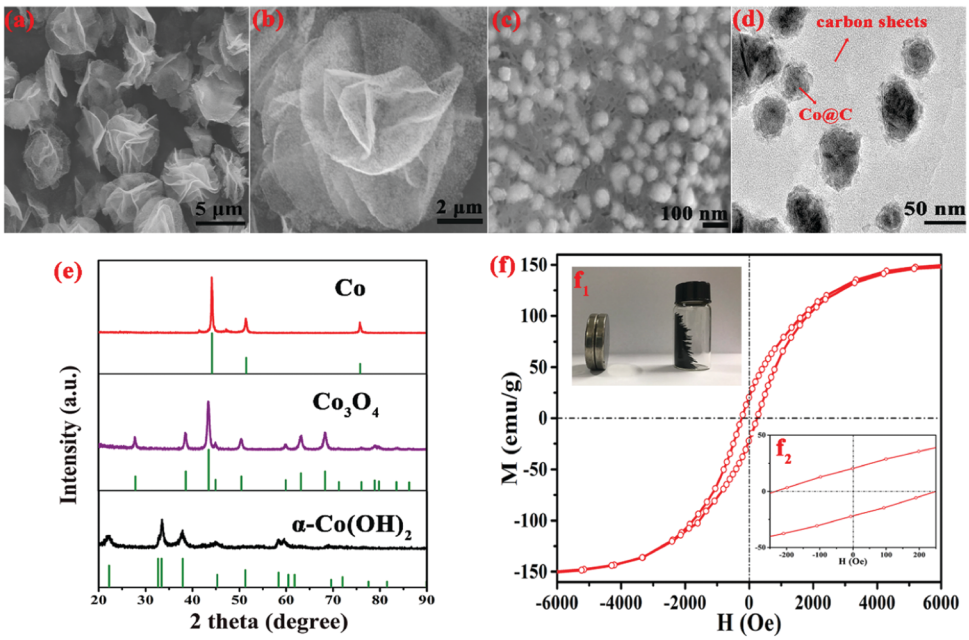

Fig. 1 (a–c) SEM images of the as-synthesized hierarchical porous Co/C crabapples with different magnifications; (d) TEM image of Co nanoparticles (NPs) on carbon sheets; (e) XRD patterns of the Co/C crabapples; and (f) field-dependent hysteresis loop of Co/C crabapples measured at room temperature. Inset f_1 indicates the strong magnetism of the Co/C crabapples. Inset f_2 is the enlarged low field hysteresis curve.

are cobalt. Meanwhile, the tortuous lattice fringe indicates a *ca.* 5 nm thick carbon layer outside of the Co nanoparticles (Fig. S1e, ESI†). The SAED pattern in Fig. S1f (ESI†) indicates that the diffraction rings correspond well to the (111), (200), and (220) planes of fcc-Co,[17] thereby confirming the successful synthesis of the hierarchical porous Co/C crabapples.

The crystal structure of the products was investigated by XRD (Fig. 1e). For the products synthesized during the solvothermal process, all diffraction peaks of the precursor were assigned to α-$Co(OH)_2$ (JCPDS No. 02-0925). After calcination treatment, the diffraction peaks at 31.2°, 36.8°, 38.5°, 44.8°, 55.6°, 59.4°, and 65.2° match well with the Co_3O_4 intermediate (JCPDS No. 42-1467). After reduction by carbon, three main peaks at 44.2°, 51.5° and 75.8° fitted well with the (200), (111) and (220) planes of Co (JCPDS Card No. 15-0806), suggesting the complete transformation of Co_3O_4 to Co. The strong and sharp peaks of the Co/C crabapples indicate that the inner cobalt nanoparticles have a high degree of crystallinity. No observed reflection of cobalt oxide indicates that the Co/C crabapple is not oxidized, owing to the protection of the carbon shell. Besides, the absent peak of carbon, see Fig. 1e, confirms the amorphous nature oft he carbon. The average grain size of the Co nanoparticles was estimated to be 32.4 nm using Scherrer's equation.[29] Raman spectra were employed to further confirm the state of carbon and graphitization degree of the Co/C crabapples. Two distinguishable peaks centered at *ca.* 1328 cm^{-1} (D band) and 1586 cm^{-1} (G band) can be observed in Fig. S3 (ESI†). The D band is associated with the lattice disorder in the sp^2-hybridized carbon atoms or amorphous carbon deposits, while the G band represents the sp^2 atoms in a 2D hexagonal graphitic lattice. The intensity ratio of D band to G band (I_D/I_G) can reflect the graphitization degree of materials.[30] A larger I_D/I_G value means a lower graphitization degree and a higher disordered degree of carbon. As shown in Fig. S3 and Table S1 (ESI†), the calculated I_D/I_G value of the Co/C crabapples (1.86) is much larger than other reported magnetic carbon materials such as Co/C nanoparticles (1.16),[25] CNF–Co composites (0.94),[17] Fe_3O_4@C nanospindles (1.22)[30] *etc.*, suggesting a quite low graphitization degree. Combining the TEM (Fig. S1, ESI†) and XRD observations (Fig. 1), the formation of Co and amorphous carbon composites was confirmed. Thermogravimetric analysis (TGA) was carried out to evaluate the carbon content in the composites. Fig. S4 (ESI†) displays the TGA curves of the Co/C crabapples characterized in air. The carbon content was calculated by using eqn (1).

$$\mathrm{wt}\%_{\mathrm{L}} = \frac{(1 - \mathrm{wt}\%_{\mathrm{carbon}} - \mathrm{wt}\%_{\mathrm{water}})}{3M_{\mathrm{Co}}} \times M_{\mathrm{Co_3O_4}} \quad (1)$$

in which $\mathrm{wt}\%_{\mathrm{L}}$ is the remaining Co_3O_4 weight percentage at 900 °C after the complete combustion of carbon, M is the molecular mass, $\mathrm{wt}\%_{\mathrm{water}}$ is the evaporation weight percentage of water adsorbed on surface that occurred before 200 °C. Hence, $\mathrm{wt}\%_{\mathrm{carbon}}$ was determined to be 18.8% and $\mathrm{wt}\%_{\mathrm{Co}}$ is 81.2 wt%. Fig. 1f displays the hysteresis loop of the samples tested at 300 K. The *M–H* curve indicates that the Co/C crabapples possess a large saturation magnetization (M_s) of 149.6 emu g^{-1} and a coercivity (H_c) of 242.8 Oe (insets Fig. 1f). The M_s value is slightly smaller than that of bulk Co (168 emu g^{-1})[14] due to the introduction of non-magnetic carbon. On the other hand, the H_c of the samples is significantly larger than that of bulk Co (10 Oe).[14] In general, H_c with a strong size-dependent effect increases first and then decreases from the peak value with increasing size of ferromagnetic particles.[31] The particle size of the H_c peak value is called the critical particle diameter (D_{cri}). According to Leslie-Pelecky's report,[31] the D_{cri} of Co (70 nm) is a little larger than that of the as-synthesized Co particles (~32.4 nm) in this work and significantly smaller than that of bulk Co. Thus, a much larger H_c value is obtained. Generally, a large H_c value is beneficial to improve the EMW absorption performance according to eqn (2)–(4):[32]

$$K = \mu_0 M_s H_c/2 \quad (2)$$

$$H_a = 4|K|/3\mu_0 M_s \quad (3)$$

$$2\pi f_r = \gamma H_a \quad (4)$$

in which K represents the magnetocrystalline anisotropy, μ_0 is the permeability constant in free space, H_a refers to the field anisotropy energy, f_r is the natural magnetic resonance frequency and γ is the gyromagnetic ratio. The large H_c results in an increased H_a, and then a higher f_r is obtained according to eqn (4).

To understand the formation process of the α-$Co(OH)_2$ crabapples, a series of time-dependent experiments was carried out with other reaction conditions unchanged. After one-hour reaction, only a flake-shaped morphology appeared with an average size of 0.5–1.0 μm (Fig. S5a, ESI†). After reacting for 2 h, small quantities of α-$Co(OH)_2$ flowers began to form with a mess of flakes (Fig. S5b, ESI†). As the reaction time increased to 3 h, the flakes assembled to form crabapple-like structures (Fig. S5c, ESI†). The crabapple-like structure was partly destroyed at a reaction time of 10 h, indicating that 10 h was too long to obtain a crabapple-like structure (Fig. S5d, ESI†). Based on the above experimental results, the formation process of the α-$Co(OH)_2$ crabapples involved a fast nucleation followed by an aggregation and growth process of primary particles, which belonged to a typical Ostwald ripening mechanism.[33,34] In our study, methanol first coordinated with Co^{2+} to form cobalt alkoxide, which became the nucleus and grew into flake-shaped particles. With further increasing the reaction time, the freshly diffused cobalt alkoxide particles spontaneously self-assembled onto the surface of a cobalt alkoxide flake, finally forming the crabapple-like structure. However, more details concerning the interactions and mechanisms still need to be explored even though various kinds of 3D flower-like structures have been prepared.[35–38] Besides, as a kind of nonionic surfactant, PVP is an important factor in influencing the size and final morphology of the α-$Co(OH)_2$ precursor, which is presented in Fig. S6 (ESI†). Numerous scattered flakes rather than α-$Co(OH)_2$ crabapples were obtained without the addition of PVP (Fig. S6a, ESI†). When 0.5 g of PVP was added, only several α-$Co(OH)_2$

spheres were observed (Fig. S6b, ESI†). As the PVP addition was increased to 1.0 g, the α-$Co(OH)_2$ crabapples with monodispersed distribution were obtained (Fig. S6c, ESI†). The crabapple-like structure became more well-defined as the PVP addition reached 2.0 g (Fig. S6d, ESI†). Such a PVP addition dependent phenomenon has been reported in the preparation of micro/nanospheres.[39–41] According to these reports, PVP molecules physically adsorbed on the surface of subunits can prohibit grain growth as well as link the subunits to form stable structures during the reaction.

The EMW absorption of the absorbers was determined by the complex permittivity ($\varepsilon_r = \varepsilon' - j\varepsilon''$) and complex permeability ($\mu_r = \mu' - j\mu''$). Fig. 2a and d shows the frequency dependence of the real part (ε') and imaginary part (ε'') of complex permittivity over 1.0–18.0 GHz for samples M_{50} and M_{30}, respectively. As observed, the ε' curve presents a decreasing tendency with negligible fluctuations from 16.9 to12.4 and 10.4 to 4.9 while ε'' increases first and then decreases gradually from the maximum value of 3.81 and 2.27 for samples M_{50} and M_{30}, respectively. Two resonance peaks including a weak peak and a strong peak located at *ca.* 9.0 GHz and 13.8 GHz for sample M_{50}, and 9.5 GHz and 16.0 GHz for M_{30}, are observed in the ε'' curves (marked by dashed circles). According to Debye theory, ε' and ε'' can be expressed as follows:[42]

$$\varepsilon' = \varepsilon_\infty + (\varepsilon_s - \varepsilon_\infty)/(1 + \omega^2\tau^2) \quad (5)$$

$$\varepsilon'' = \varepsilon_p'' + \varepsilon_c'' = (\varepsilon_s - \varepsilon_\infty)\omega\tau/(1 + \omega^2\tau^2) + \sigma/\omega\varepsilon_0 \quad (6)$$

where ε_∞ represents the relative permittivity at the high-frequency limit, ω ($\omega = 2\pi f$) represents angular frequency, τ represents polarization relaxation time, which is related to polarization of absorbers, ε_p'' represents the polarization loss, ε_c'' is the conduction loss part, and ε_s is the static permittivity. It can be concluded from eqn (5) and (6) that ε'' is determined by ε_p'' and ε_c''. As ε_c'' decreases with the increase of frequency based on eqn (6), the resonance peaks of ε'' should be mainly ascribed to polarization loss.[43] Generally, there are mainly four kinds of polarization loss, including ion and electron polarization, dipole polarization, and interface polarization.[1] Ion and electron polarization can be excluded first as they often exist at 10^3–10^6 GHz.[1] Therefore, the polarization processes mainly derive from dipole polarization and interface polarization. For the porous Co/C crabapples, a large number of space charges with uneven distributions accumulate at the heterogeneous interface between Co NPs and carbon, contributing to the interfacial polarization.[44] Secondly, the amorphous carbon sheets provide abundant defects as polarization centers, resulting in the generation of dipole polarization.[45,46] According to previous reports,[42,47] the large increase in ε'' at *ca.* 13.8 GHz for M_{50} ($\Delta\varepsilon'' = 1.3$) and 16.0 GHz for M_{30} ($\Delta\varepsilon'' = 0.9$) should be attributed to interface polarizations, and the weak resonance peaks at 9.0 GHz for M_{50} and 9.5 GHz for M_{30} are due to dipole polarizations. In addition, it can be observed that M_{30} exhibits a lower ε'' compared with M_{50} and such a decrease can be explained by the decreased conductivity of sample M_{30} according to free electron theory: $\varepsilon'' \approx \sigma/(2\pi\varepsilon_0 f)$.[21] In order to better support our conclusion, the as-prepared Co/C crabapples were treated by strong hydrochloric acid for several minutes until they lost their magnetism and the permittivity of the remaining Co/C powders was investigated, as shown in Fig. S7 (ESI†). The resonance peak of ε'' at *ca.* 14.2 GHz caused by interface polarization still exists because Co particles cannot be removed totally by acid, but it becomes rather weak as the interfaces between Co and C are damaged severely. Besides,

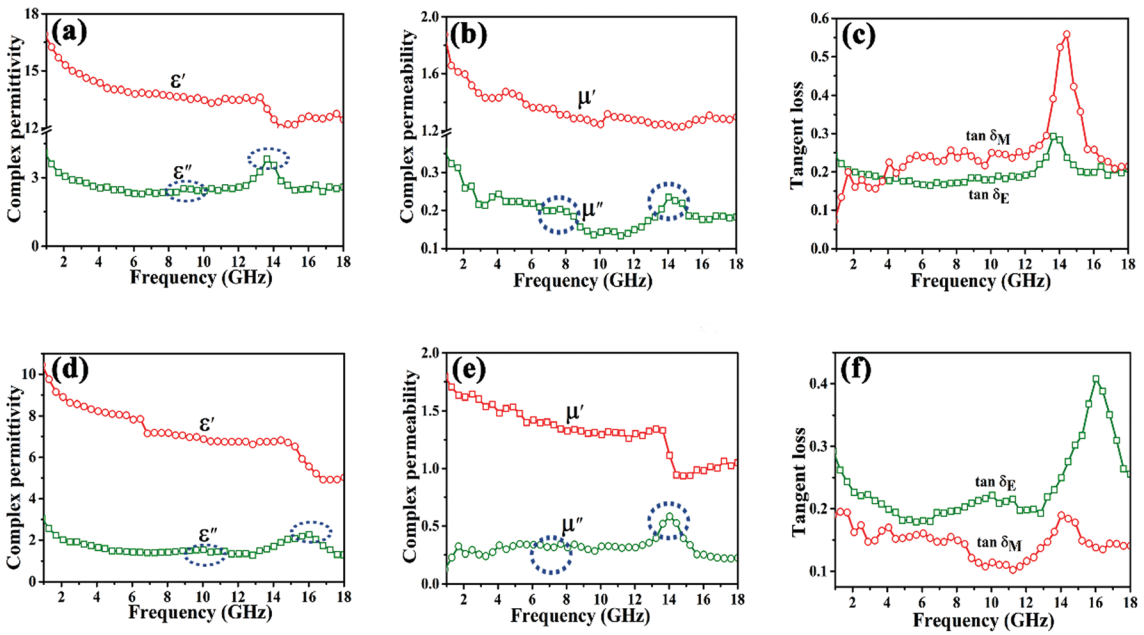

Fig. 2 Frequency dependence of (a) complex permittivity, (b) complex permeability, and (c) tangent loss for sample M_{50}; frequency dependence of (d) complex permittivity, (e) complex permeability and (f) tangent loss for sample M_{30}.

owing to the elimination of high conductivity Co particles, a rather low ε'' for the acid-treated Co/C crabapples was also observed.

Fig. 2b and e shows the changes of μ_r with frequency for the two samples. It is widely accepted that μ' and μ'' represent the storage and loss ability of magnetic energy, respectively.[29] The magnetic loss ability can be evaluated by the ratio of μ'' and μ', namely, magnetic tangent loss ($\tan\delta_M = \mu''/\mu'$), as shown in Fig. 2c and f. For sample M_{50}, μ' decreases from 1.8 to 1.3 in the range of 1–10 GHz while a weak resonance peak is observed in the μ'' curves in the range of 4–10 GHz. In the range of 12–18 GHz, μ' remains almost constant with some fluctuations and μ'' exhibits a strong resonance peak (marked in Fig. 2b). Correspondingly, an intense peak is observed in this frequency range (Fig. 2c), indicating the strong magnetic loss ability. For sample M_{30}, a sharp decrease of μ' in the frequency range of 12–18 GHz occurs while the corresponding μ'' shows a resonance peak, and the increased $\tan\delta_M$ value in Fig. 2f suggests that the dissipation process is mainly through magnetic loss. In general, the ferromagnetic loss mainly includes domain wall resonance, exchange resonance, eddy current and natural resonance.[20] The domain wall resonance exists at a low frequency (<100 MHz), and thus it can be neglected in the GHz range.[48] The eddy current loss is associated with the thickness (d) and electric conductivity (σ) of the absorbers, shown in eqn (7):[49]

$$C_0 = \mu''(\mu')^{-2}f^{-1} = 2\pi\mu d^2\sigma \quad (7)$$

If the magnetic loss just originates from eddy current loss, the C_0 value should be constant when frequency changes. Fig. S8 (ESI†) shows that C_0 significantly changes as the frequency changes, indicating that eddy current loss could be excluded. For the hierarchical porous Co/C crabapples, the fluctuation of μ'' should be attributed to natural resonance and exchange resonance. According to Aharoni's theory,[50] the exchange resonance occurs as the spherical particle size is smaller than 100 nm, attributed to the small size effect of nanocrystalline structure and surface effect.[51,52] The experimental investigations carried out by Toneguzzo *et al.* suggested that the exchange resonance occurs in a higher frequency range than that of natural resonance.[53] Therefore, the resonance peak at low frequency (below 10 GHz) for the Co/C crabapples resulted from natural resonance and the peak at high-frequency (10–18 GHz) should be ascribed to exchange resonance. In order to confirm the dominant loss mechanisms for the enhanced EMW absorption of the hierarchical porous Co/C crabapples, the comparisons of dielectric loss tangent ($\tan\delta_E = \varepsilon''/\varepsilon'$) and magnetic loss tangent ($\tan\delta_M = \mu''/\mu'$) are presented in Fig. 2c and f. For sample M_{50}, the little difference of $\tan\delta_E$ and $\tan\delta_M$ values over 1.0–12.0 GHz and 15.6–18.0 GHz (Fig. 2c) demonstrates the co-existence of dielectric and magnetic losses. From 12.0–15.6 GHz, magnetic loss rather than dielectric loss plays a more dominant role. For sample M_{30}, the much larger $\tan\delta_E$ than $\tan\delta_M$ observed in Fig. 2f indicates that dielectric loss dominates the EMW absorption. The observed results suggest that the EMW absorption mechanisms will change from magnetic loss to dielectric loss with decreasing porous Co/C crabapple loading.

The EMW absorption of the samples evaluated by RL values was calculated using the measured μ_r and ε_r based on the transmit line theory, as expressed by eqn (8) and (9):[64]

$$Z_{in} = Z_0(\mu_r/\varepsilon_r)^{1/2}\tanh\{j(2\pi fd/c)(\mu_r/\varepsilon_r)^{1/2}\} \quad (8)$$

$$RL = 20\log|(Z_{in} - Z_0)/(Z_{in} + Z_0)| \quad (9)$$

in which Z_{in} represents the input impedance of the absorber, Z_0 stands for the input impedance of air, f is the frequency, c is the light velocity, and d is the matching thickness. Fig. 3a and b shows the three-dimensional RL curves of samples M_{50} and M_{30} with the thicknesses varying from 1.0 to 5.0 mm over 1–18 GHz. For sample M_{50}, as displayed in Fig. 3a, the best RL of −56.9 dB was attained at 9.3 GHz with a matching thickness of only 1.92 mm. The RL values exceeding −10 dB (over 90% EMW absorption) were observed in a wide frequency range of 2.8–18.0 GHz with thicknesses of 1.0 to 5.0 mm. From the corresponding 2D image in Fig. 3a′, the effective bandwidth with RL < −10 dB reaches 5.9 GHz (11.2–17.1 GHz) at a thin thickness of 1.4 mm. When the thickness is as thin as 1.1 mm, the effective absorption bandwidth of 4.4 GHz (13.6–18.0 GHz) can still be achieved. For the M_{30} sample, the strongest RL peak of −26.6 dB appears at 16.0 GHz with a matching thickness of 1.84 mm (Fig. 3b) with the effective absorption bandwidth of 4.8 GHz (13.2 to 18.0 GHz) (Fig. 3b′). Located at the thickness of 2.0 mm, a broad bandwidth of 5.8 GHz is gained (12.2–18.0 GHz, Fig. 3b). Although M_{50} exhibits a larger EMW absorption intensity than M_{30} because of the much stronger magnetic loss ability of M_{50} compared to M_{30} (shown in Fig. 2c), a broad bandwidth can still be achieved at a low filling ratio of 30 wt%. Actually, both broad bandwidth and the optimal EMW are determined by impedance matching between incident EM waves and free space ($|Z_{in}/Z_0|$). An absorption peak can be observed when the $|Z_{in}/Z_0|$ value is equal to 1.0 and a broad absorption bandwidth can be gained when $|Z_{in}/Z_0|$ values are close to 1.0 in a wide frequency range. Both M_{50} and M_{30} samples are observed to have $|Z_{in}/Z_0|$ values around 1.0 in a wide frequency range in Fig. 3c and d, especially M_{50}, suggesting an excellent impedance matching level for the as-prepared porous Co/C crabapples. In order to highlight the high-performance EMW absorption of the Co/C crabapples, Table 1 summarises the EMW absorption of previously reported pure Co materials, Co/C composite absorbers and the materials reported in this study. When compared with pure cobalt absorbers and previously reported Co/C composites, the as-synthesized porous Co/C crabapples displayed greatly enhanced EMW absorption performance. The reason for the enhanced EMW absorption can be explained as follows. Owing to the complementary effect of cobalt and amorphous carbon, the obtained moderate permittivity and enhanced permeability improved the impedance matching level. Broad bandwidths were gained from the optimized impedance matching. Meanwhile, the strong magnetism of Co itself endows the composite with strong magnetic loss ability and

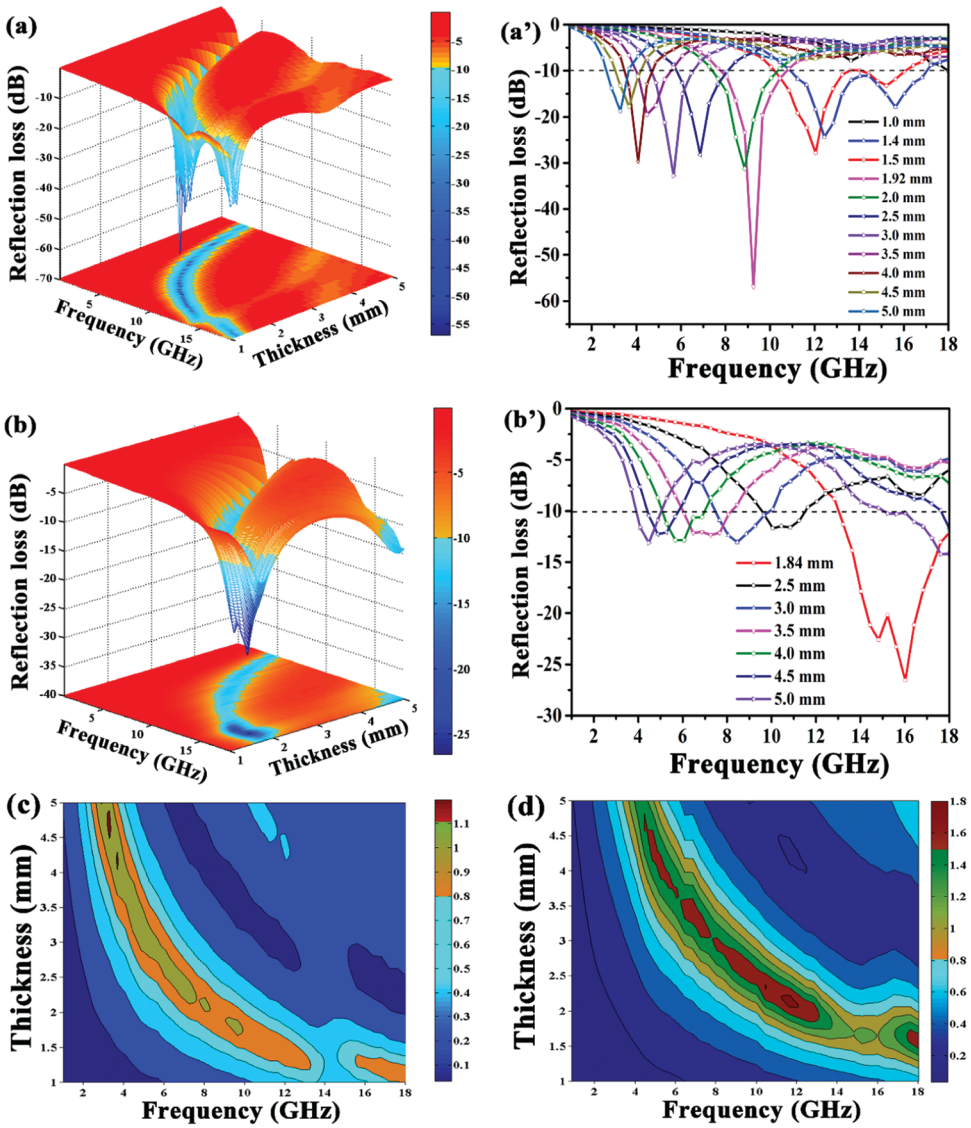

Fig. 3 (a) 3D representations and (a′) corresponding 2D RL curves with frequency and thickness for sample M_{50}. (b) 3D representations and (b′) corresponding 2D RL curves with frequency and thickness for sample M_{30}. 3D contour map of $|Z_{in}/Z_0|$ values with frequency and thickness for samples (c) M_{50} and (d) M_{30}.

makes it possible to obtain ultrathin matching thicknesses from the enlarged permeability and permittivity at a certain frequency on the basis of the quarter wavelength model $\left(d = nc/4f\sqrt{|\mu_r||\varepsilon_r|}\right)$.

Apart from the impedance matching level, the microstructures play a vital role in the EMW absorption performance. Fig. 4a and b shows the BET specific surface area (S_{BET}) and pore size distribution of the Co/C crabapples. The S_{BET} for hierarchical porous Co/C crabapples is 68.4 $m^2\ g^{-1}$, which is larger than that of the reported porous Fe@C nanocubes (50.0 $m^2\ g^{-1}$),[19] hollow porous cobalt spheres (8.8 $m^2\ g^{-1}$),[14] and Fe_3O_4/C NRs (64.27 $m^2\ g^{-1}$).[65] The dominant pore size of *ca.* 20 nm indicates the mesoporous characteristic of the Co/C crabapples. The effects of multiple components and microstructures on the enhanced EMW absorption of the hierarchical porous Co/C crabapples can be concluded from the following aspects, as shown in Fig. 4c. Firstly, the large specific surface area of the carbon sheets (shown in Fig. 4a) facilitates the high loading of Co particles, providing strong magnetic loss ability and an improved impedance matching obtained from the combination of carbon and Co particles. Secondly, the natural resonance, deriving from the uniform precession modes of magnetization vector (**M**) around the effective field (H_{eff}), contributes to the magnetic loss.[66] The existence of resonance peaks in the high frequency range (10–18 GHz, Fig. 3) indicates the exchange resonance, which also has a great effect on the magnetic loss. Thirdly, the abundant defects existing on the carbon sheets would break the balance of charge distribution, giving rise to dipole polarizations.[67] The interfaces between Co particles and carbon can produce interfacial polarization, and EM energy can be dissipated through the polarization loss. Finally, the massive pores and defects of the Co/C

Table 1 EMW absorption properties of previously reported pure Co materials and Co/C composites

	Mass fraction (wt%)	Optimal RL (dB)	Optimal thickness (mm)	Bandwidth		Ref.
				Thickness (mm)	RL < −10 dB (GHz)	
Co dendrites	65	−35.6	3.0	2.0	3.0 (7.5–10.5)	54
Fe-Co/NPC-2.0	50	−21.7	1.2	1.5	4.8 (9.2–14.0)	18
Co flowers	60	−12.3	2.0	2.0	1.7 (4.5–6.2)	55
Porous Co/C-500	40	−35.3	4.0	2.0	5.5 (12.5–18.0)	56
MWCNTs/Co	60	−37.0	5.25	2.0	1.5 (7.5–9.0)	49
Porous carbon/Co	30	−40.0	5.0	1.8	2.5 (12.0–14.5)	57
Oriented FeCo@C	—	−48.2	2.1	2.1	2.6 (5.2–7.8)	23
Co nanowires	50	−23.5	5.0	2.0	—	58
$Co_{20}Ni_{80}$ flower-like microspheres	—	−21.8	2.0	2.0	5.0 (6.0–11.0)	59
Single-shelled Co/C/PA	50	−23.2	2.0	2.0	4.8 (13.2–18.0)	60
Co/C-800	30	−39.6	2.55	2.0	3.8 (10.7–14.5)	61
CoFe@C	50	−43.5	2.5	2.0	4.4 (10.9–15.3)	62
CoNi@C nanocapsules	40	−35.0	2.0	2.0	5.1 (12.9–18.0)	63
Porous Co/C crabapples	50	**−56.9**	**1.92**	1.4	**5.9 (11.2–17.1)**	This work
Porous Co/C crabapples	30	−26.6	**1.84**	2.0	**5.8 (12.2–18.0)**	This work

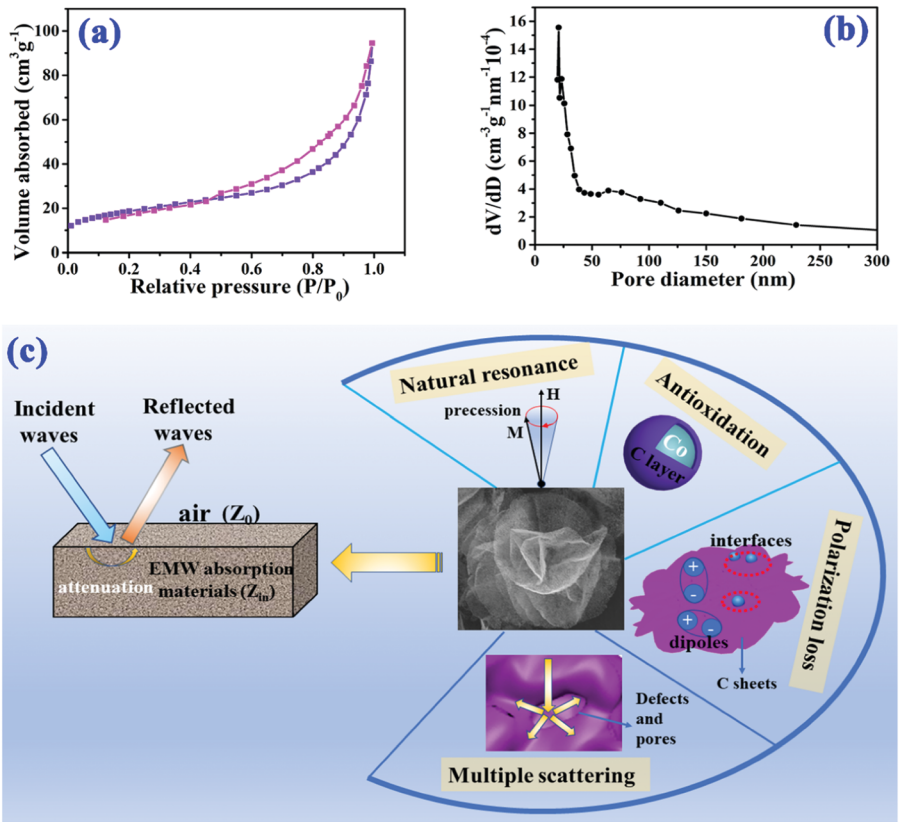

Fig. 4 (a) Nitrogen adsorption–desorption isotherms, (b) pore size distribution plot and (c) schematic representation of the EMW absorption mechanisms for hierarchical porous Co/C crabapples.

crabapples enable the occurrence of multi-scattering. When the incident EM waves strike on the defects, they can be scattered in all directions and further enhance the EMW absorption performance.[67,68] Combining an improved impedance matching with the structural advantages, the as-synthesized Co/C crabapples with high-performance EMW absorption and ultrathin absorber thickness exhibit great potential for practical applications.

4. Conclusion

Hierarchical porous Co/C crabapples were fabricated *via* a facile solvothermal reaction followed by C reduction treatment. The hierarchical porous Co/C crabapples showed improved EMW wave absorption over the pure Co absorbers and previously reported Co/C composites. A broad absorption bandwidth was achieved due to the improved impedance matching level of

porous Co/C crabapples resulting from the synergy of cobalt and carbon. The strong magnetism of cobalt itself endowed the composites with strong absorption intensity and ultrathin absorber thickness. The formed carbon layer on the Co nanoparticles enhanced the oxidation resistance. The hierarchical and porous structures of Co/C crabapples are beneficial in promoting the generation of multiple reflections and scatterings. These results indicate that this study provides a simple and facile approach to fabricate high-performance and ultrathin EMW absorbers. Compared with heavy metals,[69] ceramics[70] and less thermally stable polymers[71] and their nanocomposites,[72] the significantly improved anti-oxidation ability and the maintained high purity Co particles with high magnetization arising from the protected carbon layer make hierarchical porous Co/C crabapples attractive for other potential applications like polluted water treatment,[73] energy storage/conversion,[74] and multifunctional nanocomposites.[75]

Conflicts of interest

There are no conflicts to declare.

Acknowledgements

The authors acknowledge the financial support from the National Natural Science Foundation of China (No. 51572157) and the Natural Science Foundation of Shandong Province (ZR2016BM16).

References

1 H. Wang, L. Xiang, W. Wei, J. An, J. He, C. Gong and Y. Hou, *ACS Appl. Mater. Interfaces*, 2017, **9**, 42102–42110.
2 (*a*) L. Lv, J. Liu, H. Liu, C. Liu, Y. Lu, K. Sun, R. Fan, N. Wang, N. Lu, Z. Guo and E. K. Wujcik, *Eng. Sci.*, 2018, **2**, 26–42, DOI: 10.30919/es8d615; (*b*) L. Wang, H. Qiu, C. Liang, P. Song, Y. Han, Y. Han, J. Gu, J. Kong, D. Pan and Z. Guo, *Carbon*, 2019, **141**, 506–514; (*c*) P. Xie, B. He, F. Dang, J. Lin, R. Fan, C. Hou, H. Liu, J. Zhang, Y. Ma and Z. Guo, *J. Mater. Chem. C*, 2018, **6**, 8812–8822.
3 (*a*) N. Wu, C. Liu, D. Xu, J. Liu, W. Liu, Q. Shao and Z. Guo, *ACS Sustainable Chem. Eng.*, 2018, **6**, 12471–12480; (*b*) D. Jiang, V. Murugadoss, Y. Wang, J. Lin, T. Ding, Z. Wang, Q. Shao, C. Wang, H. Liu, N. Lu, R. Wei, S. Angaiah and Z. Guo, *Polym. Rev.*, 2019, DOI: 10.1080/15583724.2018.1546737.
4 (*a*) J. Guo, H. Song, H. Liu, C. Luo, Y. Ren, T. Ding, M. A. Khan, D. P. Young, X. Liu, X. Zhang, J. Kong and Z. Guo, *J. Mater. Chem. C*, 2017, **5**, 5334–5344; (*b*) K. Zhang, G. Li, L. Feng, N. Wang, J. Guo, K. Sun, K. Yu, J. Zeng, T. Li, Z. Guo and M. Wang, *J. Mater. Chem. C*, 2017, **5**, 9359–9369.
5 B. Zhao, J. Deng, R. Zhang, L. Liang, B. Fan, Z. Bai, G. Shao and C. B. Park, *Eng. Sci.*, 2018, **3**, 5–40, DOI: 10.30919/es8d735.
6 (*a*) C. Wang, V. Murugadoss, J. Kong, Z. He, X. Mai, Q. Shao, Y. Chen, L. Guo, C. Liu, S. Angaiah and Z. Guo, *Carbon*, 2018, **140**, 696–733; (*b*) C. Cheng, R. Fan, Z. Wang, Q. Shao, X. Guo, P. Xie, Y. Yin, Y. Zhang, L. An, Y. Lei, J. Ryu, A. Shankar and Z. Guo, *Carbon*, 2017, **125**, 103–112.
7 N. Wu, J. Qiao, J. Liu, W. Du, D. Xu and W. Liu, *Adv. Compos. Hybrid Mater.*, 2018, **1**, 149–159.
8 Z. Wang, R. Wei, J. Gu, H. Liu, C. Liu, C. Luo, J. Kong, Q. Shao, N. Wang, Z. Guo and X. Liu, *Carbon*, 2018, **139**, 1126–1135.
9 J. L. Snoek, *Physica*, 1948, **14**, 207–217.
10 J. R. Liu, M. Itoh and K. Machida, *Appl. Phys. Lett.*, 2006, **88**, 062503.
11 H. Lv, X. Liang, G. Ji, H. Zhang and Y. Du, *ACS Appl. Mater. Interfaces*, 2015, **7**, 9776–9783.
12 S. Wang, S. Peng, S. Zhong and W. Jiang, *J. Mater. Chem. C*, 2018, **6**, 9465–9474.
13 X. Zhang, G. Ji, W. Liu, X. Zhang, Q. Gao, Y. Li and Y. Du, *J. Mater. Chem. C*, 2016, **4**, 1860–1870.
14 C. He, S. Qiu, X. Wang, J. Liu, L. Luan, W. Liu, M. Itoh and K. Machida, *J. Mater. Chem.*, 2012, **22**, 22160–22166.
15 G. Tong, J. Yuan, W. Wu, Q. Hu, H. Qian, L. Li and J. Shen, *CrystEngComm*, 2012, **14**, 2071–2079.
16 P. Liu, V. M. H. Ng, Z. Yao, J. Zhou, Y. Lei, Z. Yang, H. Lv and L. B. Kong, *ACS Appl. Mater. Interfaces*, 2017, **9**, 16404–16416.
17 J. Xiang, J. Li, X. Zhang, Q. Ye, J. Xu and X. Shen, *J. Mater. Chem. A*, 2014, **2**, 16905–16914.
18 (*a*) X. Zhang, G. Ji, W. Liu, B. Quan, X. Liang, C. Shang, Y. Cheng and Y. Du, *Nanoscale*, 2015, **7**, 12932–12942; (*b*) N. Wu, D. Xu, Z. Wang, F. Wang, J. Liu, W. Liu, Q. Shao, H. Liu, Q. Gao and Z. Guo, *Carbon*, 2019, DOI: 10.1016/j.carbon.2019.01.028.
19 R. Qiang, Y. Du, H. Zhao, Y. Wang, C. Tian, Z. Li, X. Han and P. Xu, *J. Mater. Chem. A*, 2015, **3**, 13426–13434.
20 B. Quan, X. Liang, G. Ji, Y. Zhang, G. Xu and Y. Du, *ACS Appl. Mater. Interfaces*, 2017, **9**, 38814–38823.
21 X. F. Zhang, X. L. Dong, H. Huang, Y. Y. Liu, W. N. Wang, X. G. Zhu, B. Lv, J. P. Lei and C. G. Lee, *Appl. Phys. Lett.*, 2006, **89**, 053115.
22 X. Qi, Q. Hu, H. Cai, R. Xie, Z. Bai, Y. Jiang, S. Qin, W. Zhong and Y. Du, *Sci. Rep.*, 2016, **6**, 1–15.
23 Y. Zhang, P. Wang, Y. Wang, L. Qiao, T. Wang and F. Li, *J. Mater. Chem. C*, 2015, **3**, 10813–10818.
24 B. P. Singh, D. K. Saket, A. P. Singh, S. Pati, T. K. Gupta, V. N. Singh, S. R. Dhakate, S. K. Dhawan, R. K. Kotnala and R. B. Mathur, *J. Mater. Chem. A*, 2015, **3**, 13203–13209.
25 T. Liu, X. Xie, Y. Pang and S. Kobayashi, *J. Mater. Chem. C*, 2016, **4**, 1727–1735.
26 R. C. Che, L.-M. Peng, X. F. Duan, Q. Chen and X. L. Liang, *Adv. Mater.*, 2004, **16**, 401–405.
27 H. Zhao, Z. Li, N. Zhang, Y. Du, S. Li, L. Shao, D. Gao, X. Han and P. Xu, *RSC Adv.*, 2014, **4**, 30467–30470.
28 G. Pan, J. Zhu, S. Ma, G. Sun and X. Yang, *ACS Appl. Mater. Interfaces*, 2013, **5**, 12716–12724.
29 X. Zheng, J. Feng, Y. Zong, H. Miao, X. Hu, J. Bai and X. Li, *J. Mater. Chem. C*, 2015, **3**, 4452–4463.
30 X. Liu, X. Cui, Y. Chen, X. Zhang, R. Yu, G. Wang and H. Ma, *Carbon*, 2015, **95**, 870–878.

31 D. L. Leslie-Pelecky and R. D. Rieke, *Chem. Mater.*, 1996, **8**, 1770–1783.
32 C. Kittel, *Phys. Rev.*, 1948, **73**, 155–161.
33 A. R. Roosen and W. C. Carter, *Phys. A*, 1998, **261**, 232–247.
34 C. Burda, X. Chen, R. Narayanan and M. A. El-Sayed, *Chem. Rev.*, 2005, **105**, 1025–1102.
35 Y.-P. Zhao, D.-X. Ye, G.-C. Wang and T.-M. Lu, *Nano Lett.*, 2002, **2**, 351–354.
36 X.-S. Fang, C.-H. Ye, L.-D. Zhang, J.-X. Zhang, J.-W. Zhao and P. Yan, *Small*, 2005, **1**, 422–428.
37 L.-S. Zhong, J.-S. Hu, H.-P. Liang, A.-M. Cao, W.-G. Song and L.-J. Wan, *Adv. Mater.*, 2006, **18**, 2426–2431.
38 A. Chen, X. Peng, K. Koczkur and B. Miller, *Chem. Commun.*, 2004, 1964–1965.
39 F. Wang, J. Liu, J. Kong, Z. Zhang, X. Wang, M. Itoh and K. Machida, *J. Mater. Chem.*, 2011, **21**, 4314–4320.
40 S. Guo, G. Lu, S. Qiu, J. Liu, X. Wang, C. He, H. Wei, X. Yan and Z. Guo, *Nano Energy*, 2014, **9**, 41–49.
41 F. Zou, Y.-M. Chen, K. Liu, Z. Yu, W. Liang, S. M. Bhaway, M. Gao and Y. Zhu, *ACS Nano*, 2016, **10**, 377–386.
42 H.-J. Yang, W.-Q. Cao, D.-Q. Zhang, T.-J. Su, H.-L. Shi, W.-Z. Wang, J. Yuan and M.-S. Cao, *ACS Appl. Mater. Interfaces*, 2015, **7**, 7073–7077.
43 P. Wang, L. Cheng, Y. Zhang and L. Zhang, *ACS Appl. Mater. Interfaces*, 2017, **9**, 28844–28858.
44 K. Singh, A. Ohlan, V. H. Pham, B. R, S. Varshney, J. Jang, S. H. Hur, W. M. Choi, M. Kumar, S. K. Dhawan, B.-S. Kong and J. S. Chung, *Nanoscale*, 2013, **5**, 2411–2420.
45 X. L. Dong, X. F. Zhang, H. Huang and F. Zuo, *Appl. Phys. Lett.*, 2008, **92**, 013127.
46 P. C. P. Watts, W.-K. Hsu, A. Barnes and B. Chambers, *Adv. Mater.*, 2003, **15**, 600–603.
47 L. Yan, J. Liu, S. Zhao, B. Zhang, Z. Gao, H. Ge, Y. Chen, M. Cao and Y. Qin, *Nano Res.*, 2017, **10**, 1595–1607.
48 B. Zhao, X. Guo, W. Zhao, J. Deng, G. Shao, B. Fan, Z. Bai and R. Zhang, *ACS Appl. Mater. Interfaces*, 2016, **8**, 28917–28925.
49 F. Wen, F. Zhang and Z. Liu, *J. Phys. Chem. C*, 2011, **115**, 14025–14030.
50 A. Aharoni, *J. Appl. Phys.*, 1997, **81**, 830–833.
51 J. Ma, J. Li, X. Ni, X. Zhang and J. Huang, *Appl. Phys. Lett.*, 2009, **95**, 102505.
52 Q. Zhang, C. Li, Y. Chen, Z. Han, H. Wang, Z. Wang, D. Geng, W. Liu and Z. Zhang, *Appl. Phys. Lett.*, 2010, **97**, 133115.
53 P. Toneguzzo, G. Viau, O. Acher, F. Fiévet-Vincent and F. Fiévet, *Adv. Mater.*, 1998, **10**, 1032–1035.
54 X. Wang, G. Shi, F.-N. Shi, G. Xu, Y. Qi, D. Li, Z. Zhang, Y. Zhang and H. You, *RSC Adv.*, 2016, **6**, 40844–40853.
55 C. Wang, X. Han, X. Zhang, S. Hu, T. Zhang, J. Wang, Y. Du, X. Wang and P. Xu, *J. Phys. Chem. C*, 2010, **114**, 14826–14830.
56 Y. Lü, Y. Wang, H. Li, Y. Lin, Z. Jiang, Z. Xie, Q. Kuang and L. Zheng, *ACS Appl. Mater. Interfaces*, 2015, **7**, 13604–13611.
57 Q. Liu, D. Zhang and T. Fan, *Appl. Phys. Lett.*, 2008, **93**, 013110.
58 W. Chen, M. Han and L. Deng, *Phys. Rev. B: Condens. Matter Mater. Phys.*, 2010, **405**, 1484–1488.
59 Q. Liu, X. Xu, W. Xia, R. Che, C. Chen, Q. Cao and J. He, *Nanoscale*, 2015, **7**, 1736–1743.
60 L. Jiang, Z. Wang, D. Li, D. Geng, Y. Wang, J. An, J. He, W. Liu and Z. Zhang, *RSC Adv.*, 2015, **5**, 40384–40392.
61 R. Qiang, Y. Du, D. Chen, W. Ma, Y. Wang, P. Xu, J. Ma, H. Zhao and X. Han, *J. Alloys Compd.*, 2016, **681**, 384–393.
62 X. Zeng, B. Yang, L. Zhu, H. Yang and R. Yu, *RSC Adv.*, 2016, **6**, 105644–105652.
63 H. Wang, Y. Dai, W. Gong, D. Geng, S. Ma, D. Li, W. Liu and Z. Zhang, *Appl. Phys. Lett.*, 2013, **102**, 223113.
64 P. Xie, H. Li, B. He, F. Dang, J. Lin, R. Fan, C. Hou, H. Liu, J. Zhang, Y. Ma and Z. Guo, *J. Mater. Chem. C*, 2018, **6**, 8812–8822.
65 T. Wu, Y. Liu, X. Zeng, T. Cui, Y. Zhao, Y. Li and G. Tong, *ACS Appl. Mater. Interfaces*, 2016, **8**, 7370–7380.
66 Y. Li, W. Cao, J. Yuan, D. Wang and M. Cao, *J. Mater. Chem. C*, 2015, **3**, 9276–9282.
67 X. Sun, J. He, G. Li, J. Tang, T. Wang, Y. Guo and H. Xue, *J. Mater. Chem. C*, 2013, **1**, 765–777.
68 G. M. Rutter, J. N. Crain, N. P. Guisinger, T. Li, P. N. First and J. A. Stroscio, *Science*, 2007, **317**, 219–222.
69 (*a*) Y. Zhao, L. Qi, Y. Jin, K. Wang, J. Tian and P. Han, *J. Alloys Compd.*, 2015, **647**, 1104–1110; (*b*) Z. Zhao, R. Guan, J. Zhang, Z. Zhao and P. Bai, *Acta Metall. Sin.*, 2017, **30**, 66–72; (*c*) Z. Zhao, P. Bai1, R. Guan, V. Murugadoss, H. Liu, X. Wang and Z. Guo, *Mater. Sci. Eng., A*, 2018, **734**, 200–209; (*d*) Z. Zhao, R. Misra, P. Bai, J. Gao, Y. Li, R. Guan and Z. Guo, *Mater. Lett.*, 2018, **232**, 202–205; (*e*) Y. Zhao, S. Deng, H. Liu, J. Zhang, Z. Guo and H. Hou, *Comput. Mater. Sci.*, 2018, **154**, 365–370; (*f*) H. Du, Y. An, Y. Wei, L. Hou, B. Liu, H. Liu, Y. Ma, J. Zhang, N. Wang, A. Umar and Z. Guo, *Sci. Adv. Mater.*, 2018, **10**, 1063–1072.
70 (*a*) Z. Wang, H. Zhu, N. Cao, R. Du, Y. Liu and G. Zhao, *Mater. Lett.*, 2017, **186**, 274–278; (*b*) B. Kirubasankar, V. Murugadoss, J. Lin, T. Ding, M. Dong, H. Liu, J. Zhang, T. Li, N. Wang, Z. Guo and S. Angaiaha, *Nanoscale*, 2018, **10**, 20414–20425; (*c*) W. Du, X. Wang, J. Zhan, X. Sun, L. Kang, F. Jiang, X. Zhang, Q. Shao, M. Dong, H. Liu, V. Murugadoss and Z. Guo, *Electrochim. Acta*, 2019, **296**, 907–915.
71 (*a*) C. Wang, Z. He, X. Xie, X. Mai, Y. Li, T. Li, M. Zhao, C. Yan, H. Liu, E. Wujcik and Z. Guo, *Macromol. Mater. Eng.*, 2018, **303**, 1700462; (*b*) C. Wang, B. Mo, Z. He, Q. Shao, D. Pan, E. Wujick, J. Guo, X. Xie, X. Xie and Z. Guo, *J. Membr. Sci.*, 2018, **556**, 118–125; (*c*) C. Wang, B. Mo, Z. He, C. X. Zhao, L. Zhang, Q. Shao, X. Guo, E. Wujcik and Z. Guo, *Polymer*, 2018, **138**, 363–368.
72 (*a*) M. Dong, Q. Li, H. Liu, C. Liu, E. Wujcik, Q. Shao, T. Ding, X. Mai, C. Shen and Z. Guo, *Polymer*, 2018, **158**, 381–390; (*b*) Y. Qian, Y. Yuan, H. Wang, H. Liu, J. Zhang, S. Shi, Z. Guo and N. Wang, *J. Mater. Chem. A*, 2018, **6**, 24676–24685; (*c*) Y. Sheng, J. Yang, F. Wang, L. Liu, H. Liu, C. Yan and Z. Guo, *Appl. Surf. Sci.*, 2019, **465**, 154–163; (*d*) Z. Qu, M. Shi, H. Wu, Y. Liu, J. Jiang and C. Yan, *J. Power Sources*, 2019, **410–411**, 179–187; (*e*) W. Xie, X. Zhu, S. Yi,

J. Kuang, H. Cheng, W. Tang and Y. Deng, *Mater. Des.*, 2016, **90**, 38–46.

73 (*a*) H. Shindume, Z. Zhao, N. Wang, H. Liu, A. Umar, J. Zhang, T. Wu and Z. Guo, *J. Nanosci. Nanotechnol.*, 2019, **19**, 839–949; (*b*) K. Gong, Q. Hu, Y. Xiao, X. Cheng, H. Liu, N. Wang, B. Qiu and Z. Guo, *J. Mater. Chem. A*, 2018, **6**, 11119–11128; (*c*) J. Huang, Y. Li, Y. Cao, F. Peng, Y. Cao, Q. Shao, H. Liu and Z. Guo, *J. Mater. Chem. A*, 2018, **6**, 13062–13074; (*d*) K. Gong, S. Guo, Y. Zhao, Q. Hu, H. Liu, D. Sun, M. Li, B. Qiu and Z. Guo, *J. Mater. Chem. A*, 2018, **6**, 16824–16832; (*e*) J. Huang, Y. Cao, Q. Shao, X. Peng and Z. Guo, *Ind. Eng. Chem. Res.*, 2017, **56**, 10689–10701.

74 (*a*) H. Du, C. Zhao, J. Lin, Z. Hu, Q. Shao, J. Guo, B. Wang, D. Pan, E. K. Wujcik and Z. Guo, *Chem. Rec.*, 2018, **18**, 1365–1372; (*b*) M. Idrees, S. Batool, J. Kong, Q. Zhuang, H. Liu, Q. Shao, N. Lu, Y. Feng, E. K. Wujcik, Q. Gao, T. Ding, R. Wei and Z. Guo, *Electrochim. Acta*, 2019, **296**, 925–937.

75 (*a*) Y. He, S. Yang, H. Liu, Q. Shao, Q. Chen, C. Lu, Y. Jiang, C. Liu and Z. Guo, *J. Colloid Interface Sci.*, 2018, **517**, 40–51; (*b*) X. Cui, G. Zhu, Y. Pan, Q. Shao, C. Zhao, M. Dong, Y. Zhang and Z. Guo, *Polymer*, 2018, **138**, 203–210.